Macromagnetic Approach to the Modeling in Time Domain of Magnetic Losses of Ring Cores of Soft Ferrites in Power Electronics

Hari Prasad Rimal, *Student Member, IEEE*, Giulia Stornelli, Antonio Faba, *Senior Member, IEEE*, and Ermanno Cardelli, *Senior Member, IEEE*

***Abstract*—This article presents a new modeling approach capable of predicting Eddy current losses in soft ferrite cores as a function of the winding current. The proposed model is formulated in the time domain, which defines the magnetic core as a repeated regular structure of magnetic material grains and grain boundary in space. In this way, the homogenization process of the material is avoided, which is intended as the definition of a set of physical parameters of a continuous material equivalent to the real structure of the material. The distribution of the current density in the core and the core losses are computed utilizing the physical and geometric parameters of the grain of the magnetic material and of the grain boundary. To address the uncertainty in the definition of the physical and geometrical parameters of the magnetic grain and the grain boundary, a dedicated optimization procedure has been formulated, which takes into account the inaccuracy in the parameter measurement and the fact that the grain contour is an irregular surface and the boundary thickness is neither constant nor uniform. The performance assessment of the model is carried out over a broad frequency range using several experiments with a power amplifier and a dc–dc converter.**

***Index Terms*—Ferrites, finite-difference methods, loss measurement, magnetic losses, modeling.**

I. Introduction

SOFT ferrites have been firmly established as one of the most important classes of magnetic materials used in present-day power electronics equipment. Among them, manganese–zinc (MnZn) ferrites have the capability to efficiently handle high-frequency signals, which result from the combination of high magnetic permeability and low core losses. Low magnetocrystalline anisotropy and high electrical resistivity are the landmark properties of good-quality sintered MnZn ferrites [1]. MnZn ferrites are usually used as the magnetic core of switching power supplies, particularly for high-frequency switching modes. The continuous increase in the use of switching power supplies and the increase in their work frequency make it crucial to control and reduce the magnetic losses in order to improve the efficiency of the system [2], [3]. This requires a complete understanding and modeling of the underlying physical phenomenon behind the core losses and their behavior over a much broader frequency range. Peer-reviewed articles classify the total power losses occurring in the MnZn ferrite at any frequency as the sum of static losses (hysteresis) and frequency-increasing dynamic losses [4], [5], [6], [7], [8], [9], [10], [11], [12], [13], [14]. Dynamic losses consist of losses due to eddy currents and residual losses. The residual losses have been qualitatively attributed to various phenomena, viz. domain wall relaxation/resonance, dielectric losses, and damped ferromagnetic resonance [5], [6]. Currently, there is no clear understanding of how the different phenomena contribute their share to the total losses observed in the material because there is a lack of quantitative justification [6].

A series of papers have proposed an interesting way to estimate the losses inside a magnetic core for nonsinusoidal induction by further generalizing the Steinmetz formula [9], [10]. However, these approaches still have their applicability confined to a quite narrow frequency range. Some other approaches compute the frequency-independent hysteresis effects based on the permeance–capacitance analogy for system-level circuit simulation [11], [12]. This type of approach does not consider the nonuniformity of the magnetic induction distribution inside the core. A further interesting proposal is to take into account the nonuniform magnetic field by defining a functional block in the time domain, which can be implemented in PSpice [13], [14]. The functional block is based on the shape of the core, which makes the approach applicable only to the preidentified core configuration. Circuital approaches are certainly interesting, as they can be easily introduced into circuit analysis codes. In the case that a more accurate analysis is desired, albeit, at the cost of greater computational complexity, numerical approaches in the time domain based on the spatial discretization of the magnetic core are required [15], [16]. There is a fair share of papers that emphasize the dominant effect of residual losses on the total core losses beyond 1 MHz only [17], [18], [19], [20], [21]. Most of the commercial MnZn ferrites, on approaching the

Manuscript received 29 August 2022; revised 17 October 2022; accepted 9 November 2022. Date of publication 18 November 2022; date of current version 26 December 2022. Recommended for publication by Associate Editor M. Chen. *(Corresponding author: Hari Prasad Rimal.)*

Hari Prasad Rimal, Antonio Faba, and Ermanno Cardelli are with the Department of Engineering, Università degli Studi di Perugia, 06123 Perugia, Italy (e-mail: haririmal@ioe.edu.np; antonio.faba@unipg.it; ermanno.cardelli@unipg.it).

Giulia Stornelli is with the Università degli Studi di Roma Tor Vergata, 00133 Roma, Italy (e-mail: giulia.stornelli@students.uniroma2.eu).

Color versions of one or more figures in this article are available at https://doi.org/10.1109/TPEL.2022.3223184.

Digital Object Identifier 10.1109/TPEL.2022.3223184

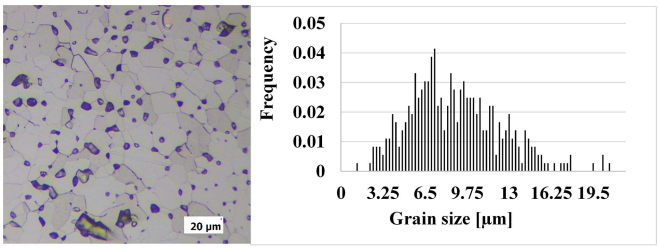

(a) (b)

Fig. 1. (a) Ferrite microstructure showing grains and the grain boundaries. (b) Grain size distribution (number of considered grain $\simeq$ 1000).

MHz frequency range, witness the frequency dispersion of the magnetic permeability. This phenomenon is correlated with the fast increase in energy losses, and this is one of the reasons behind the limited operation of such MnZn ferrite devices beyond 1 MHz. The change in the magnetic permeability according to the frequency is generally reported in the datasheet of the ferrite material.

This article deals with the modeling and computation of the magnetic losses of commercial MnZn ferrites in a broad frequency range of 100 kHz to 1 MHz, which is based on the following two premises. First, in the nominal operating frequency range of 100 kHz to 1 MHz, the dominant loss mechanism in a commercial MnZn ferrite is the conductive (eddy current) loss. Second, as specified above [17], [18], [19], [20], [21], the residual magnetic losses are relevant above 1 MHz, and the static losses are relevant below 10 kHz. The premises are verified in this article through a series of measurements. The conductive (eddy current) losses arise from both the intragranular and intergranular circulations of the Eddy currents in the material grain and the core, respectively. This study compares the quantitative significance of the intragranular losses computed using the approach mentioned in [22] and the measured static losses with the conductive losses computed using the proposed model. In the end, all of these quantities are then compared with the total measured losses for each of the analyzed cases.

The proposed model is based on knowledge of the microstructural and physical parameters of the ferrite material and of the core geometry. The model considers the fact that a magnetic core is made up of a basic composition of a grain of magnetic material of a certain shape and size surrounded by an insulating material crystallite called grain boundary. It is difficult to quantify the material's intrinsic crystallite parameters, viz. grain and grain boundary thickness, conductivity, and permittivity, from direct measurements because the real grain size, insulating grain boundary contours, and thickness are not uniform. In this study, some of the intrinsic material parameters are obtained from the direct study of the material structure, some are adopted from the related literature, and others are tuned in a small range to minimize the difference between the computed and measured losses using a suitable optimization technique. It is important to underline that the proposed model is applied here to a typical annular structure of MnZn ferrites but can be extended to any shape of the magnetic core, using suitable 3-D numerical solvers, based on finite element analysis (FEA) techniques in the time domain.

The rest of this article is organized as follows. Section II reports the findings from a study of the microstructure of the MnZn ferrite material under study, which paves the way for the model formulation. Section III presents the numerical implementation of the model in the finite-difference time domain (FDTD). The FDTD formulation presented here is not based on the classical Yee grid [23]. Section IV presents the sensitivity analysis of the model outcome to the model parameters, and Section V presents the performance assessment of the model via a series of measurements. Finally, Section VI concludes this article.

II. Modeling of MnZn Ferrite Core for Eddy Current Loss Computation

The proposed modeling technique is based mainly on the information obtained from the study of the structure of a ferrite material. In this case, we have considered a commercial MnZn ferrite, the EPCOS N30. The surface of a small section of the material under consideration was polished and etched with a solution of 33% of hydrochloric acid for 150 s. The observation of the prepared surface, using an optical microscope (Eclipse LV150NL, Nikon), showed the microstructure of the ferrite as pictured in Fig. 1(a). Fig. 1 clearly reveals the ferrite structure containing grains of different sizes, which are separated from each other by very thin grain boundaries. The grain boundary has different chemical and physical properties from ferrite grains. The grain boundaries are insulating in nature, due to which the electrical impedance of bulk ferrite exhibits frequency dispersion. Fig. 1(b) shows the grain size distribution of the ferrite sample, determined by using dedicated image analysis software (X-Plus, AlexaSoft).

The average grain size of the ferrite sample is found to be 8.75 μm with a standard deviation of 3.60 μm. As far as the grain boundaries are concerned, it is well known that they represent one of the most significant crystallographic defects affecting the electrical properties of metals, independent of their microstructure [24], [25]. Several studies have been published reporting grain boundaries as the main electron scattering source in metallic materials, which means that they affect resistivity more than surface scattering. This is also true in the case of low-dimensional materials, e.g., thin films and nanowires [26]. Based on the above-mentioned considerations, the measurement of resistivity values for different grain boundaries plays a key role, and it has been a central parameter in emerging studies involving the atomic structures, phases, and physical properties of grain boundaries [27], [28]. However, only a few studies related to the resistivity measurement of an individual grain boundary have been published, and they still do not relate electric properties with the atomic grain boundary structure [29]. This is mainly due to the difficulties in measuring grain boundaries; in fact, the atomic structure of a grain boundary is determined by its crystallography, i.e., the relative orientation between neighboring grains and the corresponding grain boundary plane, possible atomic translations, chemical composition,

and temperature [30]. Several computational studies on particular grain boundary types confirm that their structure determines the resistivity values [31]. Theoretical and experimental studies report high segregation (impurities) levels at grain boundaries, which strongly affect their properties and are directly related to resistivity [32]. On the other hand, due to the crystallographic nature and the typical size of grain boundaries, it is quite difficult to measure them with statistical significance, even by means of an electron transmission microscope. Some attempts have been made to measure the grain boundary thickness based on the 3-D reciprocal lattice of a large-angle <001> twist boundary using X-ray diffraction techniques. Such an approach allows measuring the intensity profiles of the Relrods, and the thin grain boundary region is measured, allowing the grain boundary thickness to be determined from the inverse of the width of the peaks. The detailed shape of the intensity profile for a particular Relrod depends on the atomic displacements associated with the boundary region but follows a complicated relationship [33]. It is evident that larger uncertainty lies in the measurement of grain boundary parameters.

At lower frequencies, eddy currents circulate only inside the individual ferrite grain due to the highly resistive nature of the grain boundary. At higher frequencies, eddy currents can penetrate the grain boundary, taking a larger circulation path. This change of paths creates two different natures of the dependence of total losses on the ferrite structure [16], [21]. Taking a cue from the findings of the structural study of the above-mentioned MnZn ferrite sample, a modeling technique is developed in this article to compute the dynamic losses.

The formulation to determine magnetic losses in MnZn ferrite cores is based on the definition of the basic geometry of the core structure, which approximates the actual core. The basic geometry of the material microstructure is an ordered and regular network of elementary volumes of ferrite (cubes, parallelepipeds, spheres, etc.) between which a constant thickness of the insulating grain boundary layer is interposed. This conceptualization avoids the need to apply a technique of homogenization of the material in the classical sense and is understood as the definition of a continuous material equivalent to the real structure of the material. Moreover, the two basic materials of the structure, ferrite grain and insulating grain boundary, maintain their geometrical feature and electrical characteristics. The only approximation of the proposed model is the concept of regularization, which is the hypothesis that the grains of the ferrite and the thickness of the insulating grain boundary are everywhere of the same shape and size. A more detailed description of the idealized geometry of the core structure can be found in [16].

The modeling technique is explained and discussed in detail using a toroidal-shaped ferrite core reported in Fig. 2. The width of the circular cross-section is much smaller than the radius of the toroidal core. The ferrite core is excited by a single winding, where the current $i(t)$ is applied [see Fig. 2(a)]. In this case, it can be postulated that the magnetic field strength (H) and the magnetic flux density (B) in the cross section only have the z-component. Similarly, the electric field (E) and the electric field displacement (D) are directed along the y-direction, as

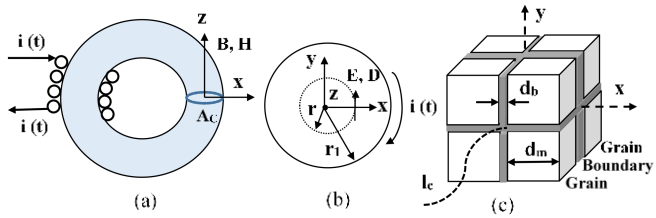

Fig. 2. (a) Toroidal ferrite core with circular cross-section A_C and exciting winding. (b) Cross section A_C. (c) Sketch of an idealized ferrite microstructure.

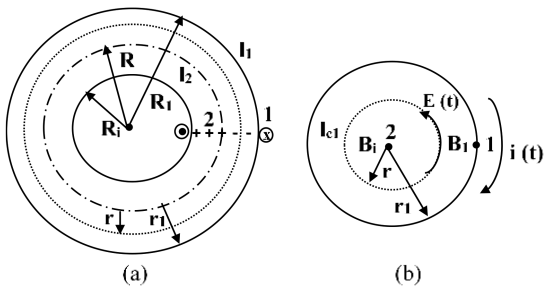

Fig. 3. Schematic of a general toroidal core to formulate the system's H and E equations. (a) Circular circumferential part. (b) Cross section.

shown in Fig. 2(b). The material is considered to be a regular succession of identical cubic grains with size d_m, surrounded by a grain boundary of constant thickness d_b, as shown in Fig. 2(c). It turns out that the magnetic induction is constant along each concentric circumference of the torus [for example, l_2 in Fig. 3(a)], and the electric field displacement is constant along each concentric circumference of the cross section [for example, l_{c1} in Fig. 3(b)]. The ratio of d_m to d_b is usually in the range of 100–1000 [3], [4]. The grain size d_m is assumed to be equal to the average grain size determined from the microstructural study of the material [see Fig. 1(b)]. The grain has electrical conductivity σ_m and magnetic permeability μ. The grain boundary is considered as the layer of material having electrical conductivity σ_b, magnetic permeability μ_0, and the electric permittivity ε. The governing equations to analyze the system in terms of E and H fields are provided by Maxwell's equations. In Fig. 2(c), l_c represents any contour of the path along which the system electromagnetic field equations are formulated, for instance, it is represented as a dotted circle in Fig. 2(b). The formulation of the proposed modeling technique is explained with reference to a ring (toroidal) core with a circular cross-section pictured in Fig. 3.

The corresponding magnetic flux density at the circular contour $r = r_1$ (outside the core) is uniform and is defined as B_1, which depends on the magnetic field strength H_1 established by the exciting current $i(t)$. Although the inside contour of the core is made up of conducting grain and insulating grain boundary, B_1 inside the core is also uniform. The boundary conditions require that the magnetic field strength be continuous in the passage from the outside (air) to the inside (ferrite grain or insulating grain boundary). The flux density at the center of the core is defined as B_i. Similarly, the electric field strength in the dielectric around the grain is E_b, and in the grain, it is E_m. They are directed along

the circular lines of the cross section of the core and are uniform for a given circular line l_{c1} [see Fig. 3(b)].

In the following, the formulation of the proposed model is explained with reference to the system shown in Fig. 3, which has a simple discretization of the core. The model formulation is generalized to a more complex core discretization in the later part of this article in Section III. The formulation is about the way of evaluating the magnetic induction in the center of the cross section of the core and the electric field strength in the intermediate circular line between the center of the cross section of the core and its contour. Maxwell's equation in integral form for the circulation of the electric field along the circular line l_{c1} at $r = 0.5r_1$ [see Fig. 3(b)] can be written as follows:

$$\oint_{l_{c1}} E.dl = -\int_S \frac{dB_{\text{avg.}}}{dt}.ds. \tag{1}$$

In (1), the magnetic flux density along the contour is approximated as the average of B_i and B_1. In consideration of the assumptions made, (1) can be rewritten as follows:

$$E_b\delta_b + E_m\delta_m = -\frac{d}{dt}\left(\frac{B_i + 0.5\,(B_1 + B_i)}{2}\right)\frac{r_1}{4}. \tag{2}$$

The parameters δ_m and δ_b in (2) are, respectively, the percentages of the grain and the grain boundary in the traversed path l_{c1}, along which the line integral in (1) is computed. The parameters δ_m and δ_b are calculated using (3), and their sum is always unity

$$\delta_b = \frac{d_b}{d_b + d_m};\quad \delta_m = \frac{d_m}{d_b + d_m};\quad \delta_m + \delta_b = 1. \tag{3}$$

Similarly, the flux densities B_1 and B_i can be related to the corresponding magnetic fields H_1 and H_i using the following equation:

$$\begin{aligned} B_1 &= \mu_o H_1 \\ \frac{dB_i}{dt} &= \mu_o\left(1 + \frac{dM_i}{dH_i}\right)\frac{dH_i}{dt}. \end{aligned} \tag{4}$$

The term *dM/dH* can be determined using modeling techniques with different degrees of approximation. The technique can be selected based on the complexity, the computational burden, and the desired degree of accuracy. Therefore, we can limit ourselves to the definition of magnetic permeability as a function of only the magnetic field, or we can introduce complex models to take into account the magnetic hysteresis, viz. the formulations based on the Preisach theory. The model formulation details along with the implementation technique for various applications can be found in [34], [35], and [36]. Now, Maxwell's equation in the integral form for the circulation of the magnetic field is written along the contour l_2 at $R = 0.5(R_1 + R_i)$ and l_1 at $R = R_1$ [see Fig. 3(a)]. Taking into account the assumptions made, we get

$$\oint_l H.dl = \int_{S_m} J_m.ds_m + \int_{S_b}\left(J_b + \varepsilon\frac{dE_b}{dt}\right).ds_b. \tag{5}$$

Analogous to what has been done for the electric field strength, J_b and J_m are the current densities across the grain boundary and the grain, respectively. Similarly, S_m and S_b are, respectively, the total areas of the metal grains and the grain boundary in the area enclosed by the contour l. The expansion of (5) along l_1 and l_2 to incorporate the area between points 1 and 2 of Fig. 3(a) results in the following:

$$\begin{aligned} &H_1.R_1 - H_i\left(\frac{R_1 + R_i}{2}\right) \\ &= -\left[\sigma_m E_m\delta_m + \left(\sigma_b E_b + \varepsilon\frac{dE_b}{\partial t}\right)\delta_b\right] \\ &\quad\times\left(\frac{R_i + 0.5\,(R_1 + R_i)}{2}\right)\left(\frac{R_1 - R_i}{2}\right). \end{aligned} \tag{6}$$

As discussed above, the magnetic field H_i has two values, H_{mi} inside the grain and H_{bi} in the grain boundary. At the interface between air and the core, the magnetic field is H_1. They can be related using the following equation:

$$\begin{aligned} H_1 &= \frac{Ni}{2\pi R_1} = \delta_m H_{mi} + \delta_b H_{bi} \\ H_{bi} &= \mu_r H_{mi} \end{aligned} \tag{7}$$

where μ_r is the relative magnetic permeability of the ferrite material and N is the total number of turns in the exciting coil.

Similarly, we can write the continuity relation at any grain boundary as follows:

$$\int_{Am}\sigma_m E_m.ds = \int_{Am}\left(\sigma_b E_b + \varepsilon\frac{dE_b}{dt}\right).ds \tag{8}$$

where A_m is the interface grain-dielectric area along the contour l_C, as shown in Fig. 2(b). Therefore, we get

$$\sigma_m E_m = \sigma_b E_b + \varepsilon\frac{dE_b}{dt}. \tag{9}$$

Equations (2) and (6) can be expressed in terms of E_b, H_{m1}, and H_{mi} using (3), (4), (7), and (9) as follows:

$$\begin{aligned} &E_b\left(\delta_b + \frac{\sigma_b}{\sigma_m}\delta_m\right) + \frac{\varepsilon}{\sigma_m}\delta_m\frac{dE_b}{dt} \\ &= -\left[\frac{\mu_o}{16}\frac{dH_1}{dt} + \frac{3\mu_o}{16}\left(1 + \frac{dM_i}{dH_i}\right)\frac{dH_i}{dt}\right]r_1 \end{aligned} \tag{10}$$

$$\begin{aligned} &H_{m1}\left(\delta_m + \mu_r\delta_b\right)R_1 - H_{mi}\left(\delta_m + \mu_r\delta_b\right)\left(\frac{R_i + R_1}{2}\right) \\ &= -\left(\sigma_b E_b + \varepsilon\frac{dE_b}{dt}\right)(R_1 - R_i)\left(\frac{R_1 + 3R_i}{8}\right). \end{aligned} \tag{11}$$

The resulting (10) and (11) contain only two unknown quantities, E_b and H_{mi}. Their solution can be evaluated for the known magnetic field H_{m1} at the core–air interface, i.e., at point 1 in Fig. 3(b). H_{m1} is determined from the known input current $i(t)$ using (12). The eddy current power losses P_E occurring inside the material is the concerned output of the model, which is calculated from the current densities at the grain and the grain boundary using (13). In (13), V is the volume of the ferrite core and J_m and J_b are the current densities defined in (5)

$$H_{m1}(t). = \frac{Ni(t)}{2\pi R_1}\frac{1}{(\delta_m + \mu_r\delta_b)} \tag{12}$$

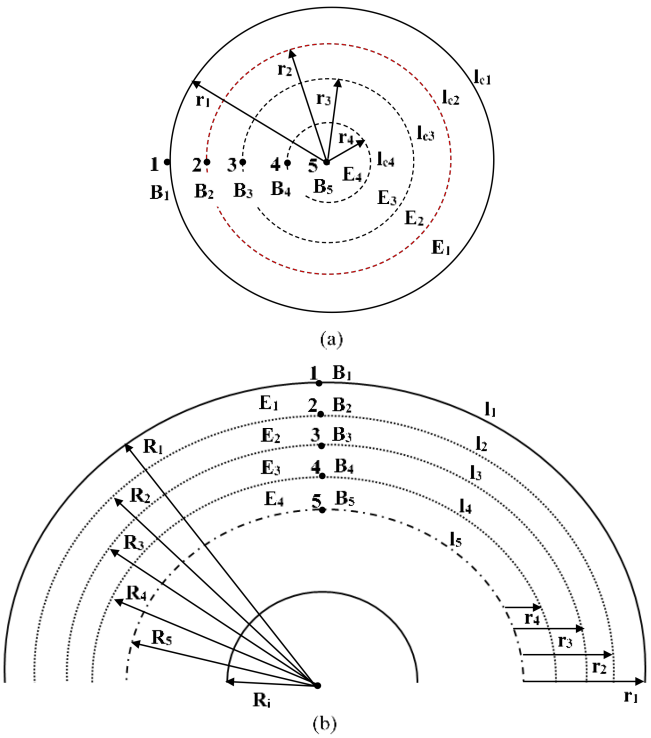

Fig. 4. Toroidal core with five elementary rings to formulate the system's *H* and *E* equations. (a) Cross section. (b) Circular circumferential part.

$$P_E = \int_V \left(\frac{J_m^2}{\sigma_m} + \frac{J_b^2}{\sigma_b} \right) dv. \tag{13}$$

III. FDTD Scheme for the Numerical Implementation of the Model

The example discussed in the previous section served to illustrate the proposed approach. If better accuracy is desired, it is necessary to calculate the values of the electric and magnetic fields and the density of the eddy currents at a larger number of points inside the core. Therefore, a less coarse discretization of the geometry is necessary. The numerical implementation of the proposed model is necessary to assess the performance of the model in predicting the desired quantities. The numerical implementation is carried out using an FDTD formulation [37]. The FDTD formulation can cover a wide frequency range and can account adequately for nonlinearity and hysteresis in a relatively easier way [38]. The ability of the above-discussed approach to accurately predict the *E* and *H* quantities inside the core greatly depends on the number of elementary ring sections (*n*) to be considered in the FDTD modeling. For instance, the toroidal core reported in Fig. 2, divided into four elemental ring sections, is reported in Fig. 4. The ring section between the points 1–2, 2–3, 3–4, and 4–5 defines four elemental ring sections (n = *4*). The electric fields E_1 to E_4 are defined for each elemental ring section and are uniform inside the corresponding ring sections. The flux densities B_1 to B_5 are defined at points 1–5, i.e., the boundary of each elemental ring and at the core center, respectively. The governing *H* and *E* equations for the system reported in Fig. 4 are obtained by expanding (1) along the contours l_{c1}– l_{c4}, and (5) along the contours l_1–l_5, which are reported in the following equations:

$$2\pi\left(\tfrac{r_1+r_2}{2}\right)E_{b1}\delta_b + 2\pi\left(\tfrac{r_1+r_2}{2}\right)\left(\tfrac{\sigma_b}{\sigma_m}E_{b1} + \tfrac{\varepsilon}{\sigma_m}\tfrac{\Delta E_{b1}}{\Delta t}\right)\delta_m = -\tfrac{\Delta}{\Delta t}\left(\tfrac{B_1+3B_2+2B_3+2B_4+2B_5}{10}\right)\pi\left(\tfrac{r_1+r_2}{2}\right)^2 \tag{14}$$

$$2\pi\left(\tfrac{r_2+r_3}{2}\right)E_{b2}\delta_b + 2\pi\left(\tfrac{r_2+r_3}{2}\right)\left(\tfrac{\sigma_b}{\sigma_m}E_{b2} + \tfrac{\varepsilon}{\sigma_m}\tfrac{\Delta E_{b2}}{\Delta t}\right)\delta_m = -\tfrac{\Delta}{\Delta t}\left(\tfrac{B_2+3B_3+2B_4+2B_5}{8}\right)\pi\left(\tfrac{r_3+r_2}{2}\right)^2 \tag{15}$$

$$2\pi\left(\tfrac{r_4+r_3}{2}\right)E_{b3}\delta_b + 2\pi\left(\tfrac{r_4+r_3}{2}\right)\left(\tfrac{\sigma_b}{\sigma_m}E_{b3} + \tfrac{\varepsilon}{\sigma_m}\tfrac{\Delta E_{b3}}{\Delta t}\right)\delta_m = -\tfrac{\Delta}{\Delta t}\left(\tfrac{B_3+3B_4+2B_5}{6}\right)\pi\left(\tfrac{r_3+r_4}{2}\right)^2 \tag{16}$$

$$2\pi\left(\tfrac{r_4}{2}\right)E_{b4}\delta_b + 2\pi\left(\tfrac{r_4}{2}\right)\left(\tfrac{\sigma_b}{\sigma_m}E_{b4} + \tfrac{\varepsilon}{\sigma_m}\tfrac{\Delta E_{b4}}{\Delta t}\right)\delta_m = -\tfrac{\Delta}{\Delta t}\left(\tfrac{B_4+3B_5}{4}\right)\pi\left(\tfrac{r_4}{2}\right)^2. \tag{17}$$

The magnetic flux densities B_1–B_5 in (14)–(17) can be expressed in terms of the magnetic fields H_{m1}–H_{m5} across metal grains in each elementary section using (4) and (7). The solution of (14)–(21) results in the quantities E_{b1}, E_{b2}, E_{b3}, E_{b4}, H_{m2}, H_{m3}, H_{m4}, and H_{m5}. Here, E_{b1}–E_{b4} are the electric field quantities across the grain boundary, and H_{m2}–H_{m5} are the magnetic field quantities across the metal grains. The aforementioned example can be extended to any ring geometry with any number of elementary ring sections (*n*)

$$H_{m1}(\delta_m + \mu_r\delta_b)2\pi R_1 - H_{m2}(\delta_m + \mu_r\delta_b)2\pi R_2 = -\left[\left(\sigma_b E_{b1} + \varepsilon\tfrac{\Delta E_{b1}}{\Delta t}\right)\right]\tfrac{2\pi(R_2+R_1)}{2}(R_1 - R_2) \tag{18}$$

$$H_{m2}(\delta_m + \mu_r\delta_b)2\pi R_2 - H_{m3}(\delta_m + \mu_r\delta_b)2\pi R_3 = -\left[\left(\sigma_b E_{b2} + \varepsilon\tfrac{\Delta E_{b2}}{\Delta t}\right)\right]\tfrac{2\pi(R_2+R_3)}{2}(R_2 - R_3) \tag{19}$$

$$H_{m3}(\delta_m + \mu_r\delta_b)2\pi R_3 - H_{m4}(\delta_m + \mu_r\delta_b)2\pi R_4 = -\left[\left(\sigma_b E_{b3} + \varepsilon\tfrac{\Delta E_{b3}}{\Delta t}\right)\right]\tfrac{2\pi(R_4+R_3)}{2}(R_3 - R_4) \tag{20}$$

$$H_{m4}(\delta_m + \mu_r\delta_b)2\pi R_4 - H_{m5}(\delta_m + \mu_r\delta_b)2\pi R_5 = -\left[\left(\sigma_b E_{b4} + \varepsilon\tfrac{\Delta E_{b4}}{\Delta t}\right)\right]\tfrac{2\pi(R_4+R_5)}{2}(R_4 - R_5). \tag{21}$$

IV. Model Parameter Sensitivity Analysis

It is reasonable to expect that by increasing the number of ring sections, the numerical result will be more accurate. However, increasing the number of ring sections indefinitely involves a higher computational cost. It is appropriate to establish the optimal choice of *n*, which is the value of *n* at which the result does not change appreciably. First, a sensitivity study of the model output to the number of ring sections was conducted using the nominal values of the ferrite intrinsic parameters reported in Table I. Some of the parameters have been taken from [39]. The eddy current losses given by (13) have been computed in the frequency range from 100 kHz to 1 MHz for a sinusoidal current input of 1 A. The choice of the magnitude of the input current is not based on any specific reason, as the findings presented in this section remain unaltered for the input current magnitude other

TABLE I
SIMULATION PARAMETERS

Parameters	Nominal Values	Optimized values
Radius of the cross section (r_i)	0.0035 m	0.0035 m
External Radius of the toroidal core (R_e)	17 e-3 m	17 e-3 m
Internal Radius of the toroidal core (R_i)	10 e-3 m	10 e-3 m
Conductivity of grain (σ_m) *	1000 S/m	1100 S/m
Conductivity of grain boundary (σ_b) *	1e-04 S/m	3.5e-04 S/m
Average grain size (d_m)	8.35 μm	8.35 μm
Thickness of grain boundary layer (d_b) *	0.1 nm	0.9 nm
Permittivity of the grain boundary (ε) *	$10\varepsilon_o$	$7\varepsilon_o$
Free space permeability (μ_o)	$4\pi \times 10^{-7}$	$4\pi \times 10^{-7}$
Relative permeability (μ_r)	4300	4300
Number of turns (N)	3	3
Number of elementary ring sections (n)	30	30

* Taken from [37] and subjected to optimization

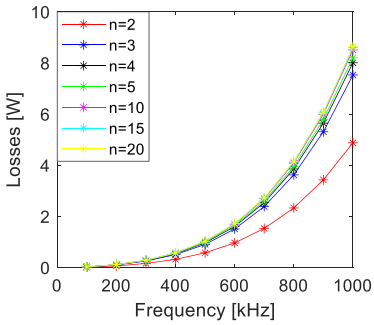

Fig. 5. Computed eddy current power losses for different numbers of elementary ring sections in the model formulation over the frequency range of 100 kHz to 1 MHz.

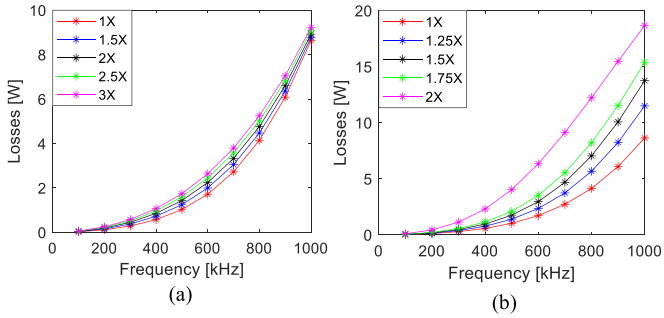

Fig. 6. Variation of the computed losses with the variation of σ_b (a) and d_m (b) over the frequency range of 100 kHz to 1 MHz.

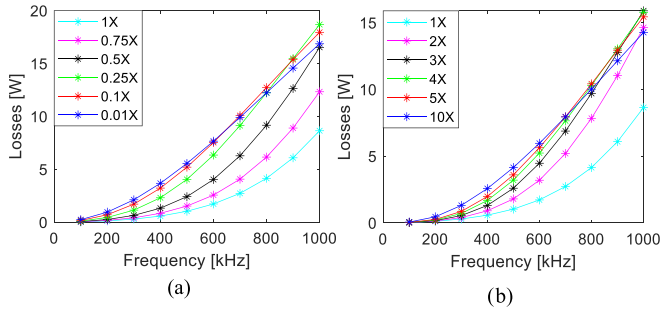

Fig. 7. Variation of the computed losses with the variation of d_b (a) and ε (b) over the frequency range of 100 kHz to 1 MHz.

than 1 A. The computed results versus the number of elementary ring sections used in the discretization are reported in Fig. 5.

It is evident in Fig. 5 that the change of the computed losses versus n decreases with the increase of n in the frequency range of 100 kHz to 1 MHz. We have found that the results computed for discretization with a number of elementary ring sections higher than 20 are practically the same, and the numerical solution converges to that. In this article, the sensitivity analysis of the model to the geometrical and electrical parameters of the core material has been performed using the value of $n = 20$. The losses computed by the model depend on the parameters σ_m, σ_b, d_m, d_b, and ε, but their values cannot be measured with absolute certainty. Among these five parameters, the range of values specified in the literature for the parameters σ_m and d_m gives the idea that these two parameters can be measured with reasonable accuracy, whereas a larger uncertainty looms around the measurement of the remaining three parameters. Again, the model sensitivity analysis has been performed to see how the eddy current losses given by (13) vary with the change in one of the above-mentioned parameters while the other parameters remain constant at the nominal values of ferrite intrinsic parameters presented in Table I. The knowledge from sensitivity analysis helps in the possible use of optimization techniques to best tune the model outcome by adjusting the more uncertain parameters within a certain range of nominal values.

The change of the computed losses versus the conductivity of the grain boundary σ_b is reported in Fig. 6(a). The parameter σ_b has been increased up to threefold with a 50% increase over the nominal value in each successive step. As expected, the computed eddy current losses increase with the increase in the value of σ_b in the entire frequency range of 100 kHz to 1 MHz. However, the increment in losses is small, so the sensitivity of computed losses is lower for this parameter. The sensitivity of computed losses to the grain size is reported in Fig. 6(b). The parameter d_m has been increased up to twofold with a 25% increase over the nominal value in each successive step. The sensitivity of computed losses to the parameter d_m is higher as compared to its sensitivity to the parameter σ_b. In this case, the losses vary appreciably depending on the parameter d_m, which is not constant but can be determined experimentally with accuracy using the technique described in Section II. For this parameter, it did not seem theoretically correct, at least at this point of the research, to determine a value using optimization techniques and experimental results, given the good accuracy with which it was possible to determine its value experimentally.

Fig. 7 reports the sensitivity of the computed losses to the thickness of grain boundary d_b and its electrical permittivity ε. In this case, the losses vary appreciably with the value of the parameter. In addition, the thickness of the dielectric (grain boundary) between the grains is not constant and is difficult to measure. The composition of the dielectric material is also difficult to define, and its dielectric permittivity is difficult to measure with accuracy. This suggests the opportunity to carry out special optimization studies of these parameters by appropriately using the appropriate experimental data.

TABLE II
EQUIPMENT FOR POWER LOSS MEASUREMENTS UNDER SINUSOIDAL EXCITATIONS

Equipment	Manufacturer and model
Signal Generator (A)	ROHDE & SCHWARZ©, model SMY 01
Power Amplifier (B)	IFI©, model M406
Digital Oscilloscope (C)	Siglent©, model 5054X, SP3050A
Voltage probe (E)	Siglent©, model SP3050A
Current Probe (D)	Pearson Electronics©, model 3525
Ferrite core (F)	EPCOS©, model N30 MnZn

V. MEASURED LOSSES AND THE MODEL ASSESSMENT

The experimental verification of the proposed modeling technique is done through the comparison of the computed results with a series of losses measured at different values of the peak flux density. Dynamic losses measured at the peak flux density of 10 mT have been used to tune the model parameters to find the best fit between the computed and measured losses. The pattern search optimization technique has been used to tune the parameters, viz. σ_m, σ_b, d_b, and ε, in a small range by minimizing the objective function subjected to the constraints of (22). The objective function is the sum of the square of the difference between the computed and measured dynamic losses in the frequency range of 100 kHz to 1 MHz [40]. In (22), k represents a particular frequency in the frequency range of 100 kHz to 1 MHz. Similarly, $P_E{}^k$ is the core loss calculated from (13) at frequency k, and $P_M{}^k$ is the core loss measured at frequency k

$$\begin{aligned} &\min \sum_{k=100\text{kHz}}^{1\text{MHz}} \left\{P_E^k(\sigma_m,\sigma_b,d_b,\varepsilon) - P_M^k\right\}^2 \\ &\text{Subject to} \\ &800 \le \sigma_m \le 1200\ (\text{S/m}) \\ &5\times10^{-5} \le \sigma_b \le 5\times10^{-4}\ (\text{S/m}) \\ &0.1\text{nm} \le d_b \le 1\ \text{nm} \\ &5\varepsilon_\circ \le \varepsilon \le 15\varepsilon_\circ \end{aligned} \tag{22}$$

The model parameters obtained from the optimization process are then used to compute the losses at the peak flux densities higher or lower than 10 mT, viz. 5 mT, 15 mT, and 20 mT. The measured input current at each frequency is used as an input to the model to compute the losses.

The schematic and the measurement setup used to measure the total power losses in the ferrite material are reported in Fig. 8. In Fig. 8(b), A is the signal generator to provide the desired reference signal to command the power amplifier, and B is the power amplifier with (10 kHz to 220 MHz) frequency range used to excite the toroidal ferrite core. The current in the magnetizing winding and the induced voltage across the search coil are recorded using a digital oscilloscope having a bandwidth of 500 MHz and a 5 GS/s sample rate. The input current is acquired using a high-precision current probe having a bandwidth of 5 Hz to 15 MHz and a sensitivity of 0.1 V/A. The voltage across the open terminal is acquired using a passive voltage probe having a 500 MHz bandwidth and an attenuation factor of 1:10. The specifications of the equipment are reported in Table II. The time-series data of the current and voltage recorded by *Ch1* and *Ch2* of the digital oscilloscope are used

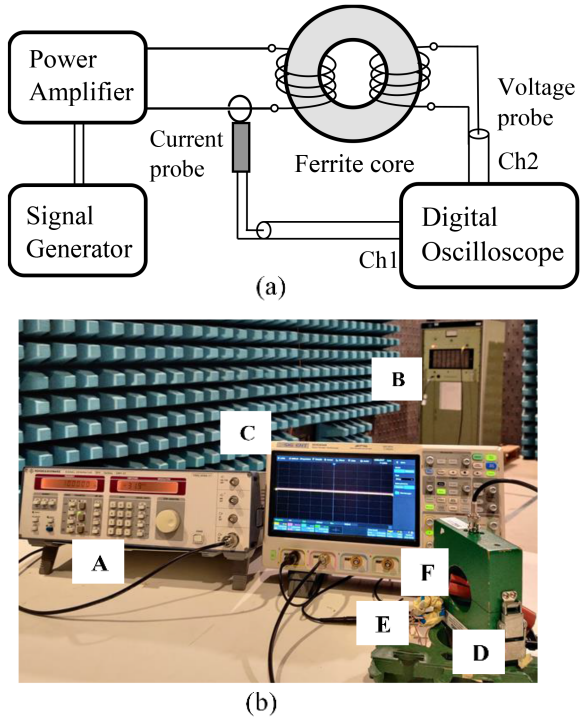

Fig. 8. Schematic diagram (a) and the measurement setup (b) used for the measurement of total core losses.

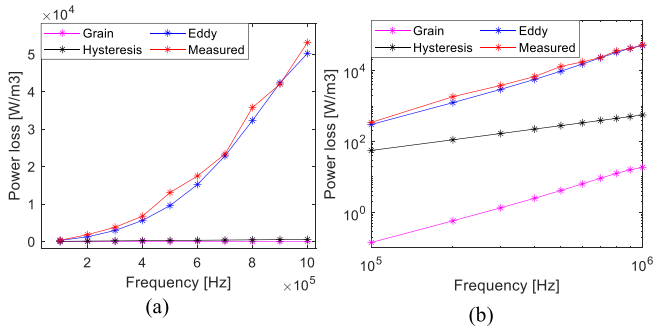

Fig. 9. At 10 mT, the eddy current losses inside grains, measured static losses (hysteresis), eddy current losses in the core, and the total measured losses represented in the linear scale (a) and the log scale (b).

to determine the applied magnetic field and average flux density in the ferrite core [36]. The area of a hysteresis loop plotted using the measured field and flux density gives the total energy loss occurring in the unit volume of the ferrite core at a given frequency.

Fig. 9 reports a comparative analysis of various losses per unit volume occurring in the given ferrite at the peak flux density of 10 mT. The losses reported are the eddy current losses inside grains computed using the approach mentioned in [22], the measured static losses in the core, the total measured losses in the core, and the proposed model computed eddy current losses in the core. Fig. 9(b) clearly depicts the contribution of the various losses to the total measured losses, where the ratio of total measured losses to the eddy current losses inside grains is in the order of 1000, whereas that to the measured static loss is in the order of 100.

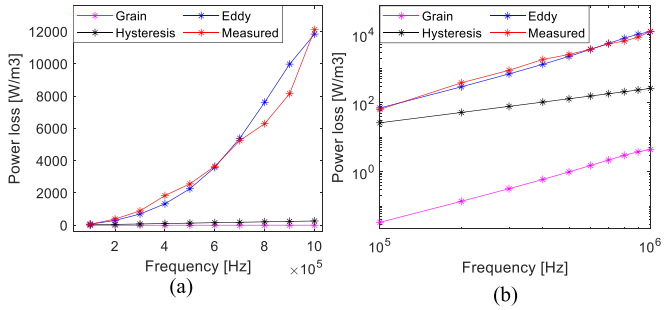

Fig. 10. At 5 mT, the eddy current losses inside grains, measured static losses (hysteresis), eddy current losses in the core, and the total measured losses represented in the linear scale (a) and the log scale (b).

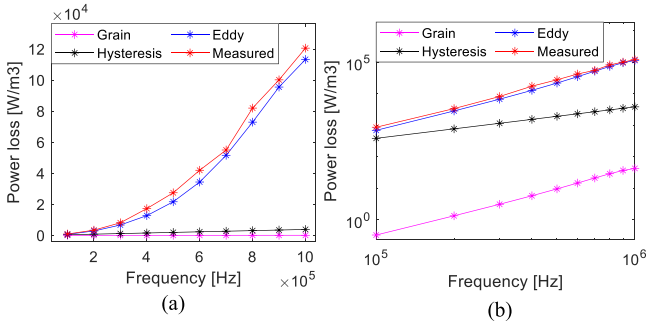

Fig. 11. At 15 mT, the eddy current losses inside grains, measured static losses (hysteresis), eddy current losses in the core, and the total measured losses represented in the linear scale (a) and the log scale (b).

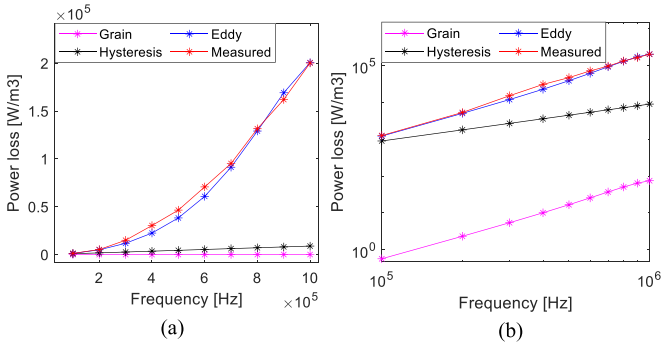

Fig. 12. At 20 mT, the eddy current losses inside grains, measured static losses (hysteresis), eddy current losses in the core, and the total measured losses represented in the linear scale (a) and the log scale (b).

Similarly, Figs. 10–12 report similar quantities at peak flux densities of 5, 15, and 20 mT, respectively. The maximum percentage difference between the computed and the measured total losses is found to be 9.87%, whereas the average percentage difference between the measured and the computed loss is 5.23%. The computed and total measured losses are in good agreement with each other. The comparison of the results confirms that once the model parameters have been identified, the variation of the excitation current has no effect on the model accuracy.

In the given frequency range, it is evident from the results that in each of the analyzed cases, the static losses and the losses inside grains are negligible as compared to the total core loss. The results of Figs. 9–12 firmly establish the premises mentioned in Section I. The performance of the proposed model

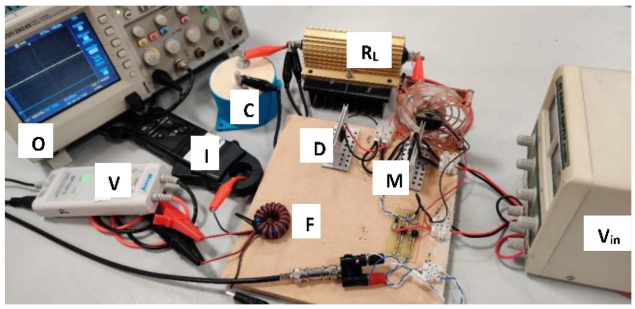

Fig. 13. Measurement setup for the measurement of total losses in the filter inductor of dc–dc buck converter.

TABLE III
EQUIPMENT FOR POWER LOSS MEASUREMENTS IN THE DC–DC BUCK CONVERTER

Equipment	Manufacturer and model
DC power supply (V_{in})	Hopewell©, model DF1730SB-5A
Ferrite core Inductor (F)	EPCOS© N30 (see table I) with 15 turns
Digital Oscilloscope (O)	Siglent©, model 5054X, SP3050A
Differential voltage probe (V)	Micsig©, model DP10013
Current Probe (I)	ROHDE & SCHWARZ©, model RT-ZC03
Load resistor (R_L)	10 Ω
Output capacitor (C)	100 μF, ICAR ITALY©, model LNK-P2X
Switching Frequency	100 kHz

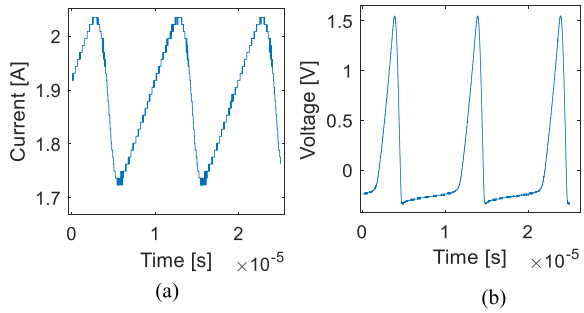

Fig. 14. Measured current through the ferrite core inductor (a) and the measured voltage across the secondary coil of the ferrite core inductor (b) of the dc–dc buck converter operating at a 66% duty ratio.

is also evaluated for the same ferrite core via a dc–dc buck converter. The ferrite core inductor is used as a filter inductor in the buck converter circuit. The converter scheme and the list of components are reported in Fig. 13 and Table III. In Fig. 13, V_{in} is the input voltage to the buck converter. Similarly, D, M, R_L, and C are the diode, MOSFET switch, load resistor, and output filter capacitor, respectively. The current probe I and the differential voltage probe V are, respectively, used to measure the current and voltage of the filter inductor F. The oscilloscope O is used to acquire and record the signals from the voltage and current probes.

As an example, the current through the inductor and the voltage across the secondary coil of the inductor for the 66% duty ratio are reported in Fig. 14. The losses occurring inside the inductor core have been analyzed for different values of the percentual ripple content of the input current, which in this article is expressed as the ratio of peak-to-peak inductor ripple current to the average inductor current, obtained by varying the converter duty ratio. The computed and measured losses inside

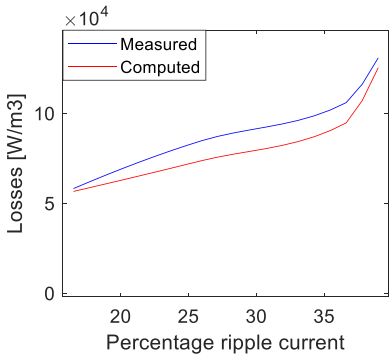

Fig. 15. Computed and measured losses for the ferrite core inductor for different values of the percentage ripple.

the inductor core as a function of the percentage ripple current are reported in Fig. 15(a). The maximum percentage difference between the computed and the measured total losses is found to be 9.23%, whereas the average percentage difference between the measured and the computed loss is 5.62%. The computed and total measured losses are in good agreement with each other. The losses inside the inductor core increase with the increase in the ripple content of the input current.

VI. Conclusion

In this work, a new modeling technique suitable for predicting the dynamic losses in ferrite cores has been presented. The proposed model is formulated in the time domain and is based on the possibility of defining the magnetic core as a regular structure of magnetic material grains and grain boundary, which are repeated in space. The microstructural composition of the material is taken into account, which avoids the complete homogenization of the ferrite material. The model utilizes the geometrical and crystallite parameters of the ferrite core. A proper analysis is done to evaluate the sensitivity of the model parameters to the computed losses. The core losses measured with sinusoidal excitation have been used to optimize the model parameters. The pattern search optimization technique has been used to tune the model parameters in a small range around their standard value. Compared to the methodologies for the determination of dynamic magnetic losses proposed by other authors, the proposed model differs due to the following.

1) It takes into account the conduction losses in the magnetic grain and the grain boundary with a physical model.
2) It allows us to take into account the nonuniform distribution of magnetic induction in the magnetic core.
3) It can consider any current versus time, including distorted periodic forms and transients.

Furthermore, once the geometric and physical parameters of the model have been determined, the calculation of the losses is very fast. Finally, the calculation can be quickly and easily extended to a whole family of cores of the same material and shape by only changing the dimensions of the core.

Experimental validation of the model has been done by comparing the computed losses and the losses measured under several different values of peak flux density using a power amplifier and a power converter. The negligible influence of losses due to static hysteresis and induced currents inside the grains of the magnetic material has been discussed for the investigated frequency range. The computed results show good agreement with the measured ones in the broad frequency range of 100 kHz to 1 MHz. The successful validation of the model creates a premise to use the model in predicting the losses in the ferrite core at the dynamic conditions, where conductive losses are a major contributor to the total losses. Therefore, this work can be considered a valid contribution to this research field. Confirmations of the validity of the presented approach are expected by extending it to higher magnetic induction values and to sintered materials of different compositions.

References

[1] J. Smit, *Ferrites*. Eindhoven, The Netherlands: Philips Technical Library, 1959, pp. 162–168.
[2] G. Stornelli et al., "Properties of additively manufactured electric steel powder cores with increased Si content," *Materials*, vol. 14, no. 6, 2021, Art. no. 1489.
[3] K. Takadate, Y. Yamamoto, A. Makino, T. Yamaguchi, and I. Sasada, "Fine grained Mn–Zn ferrite for high frequency driving," *J. Appl. Phys.*, vol. 83, no. 11, pp. 6861–6863, 1998.
[4] J. B. Goodenough, "Summary of losses in magnetic materials," *IEEE Trans. Magn.*, vol. 38, no. 5, pp. 3398–3408, Sep. 2002, doi: 10.1109/TMAG.2002.802741.
[5] H. Suhl, "Theory of the magnetic damping constant," *IEEE Trans. Magn.*, vol. 34, no. 4, pp. 1834–1838, Jul. 1998.
[6] C. Beatrice and F. Fiorillo, "Measurement and prediction of magnetic losses in Mn–Zn ferrites from DC to the megahertz range," *IEEE Trans. Magn.*, vol. 42, no. 10, pp. 2867–2869, Oct. 2006.
[7] F. Fiorillo, C. Beatrice, O. Bottauscio, and E. Carmi, "Eddy-current losses in Mn–Zn ferrites," *IEEE Trans. Magn.*, vol. 50, no. 1, Jan. 2014, Art. no. 6300109, doi: 10.1109/TMAG.2013.2279878.
[8] J. Muhlethaler, J. Biela, J. W. Kolar, and A. Ecklebe, "Improved core-loss calculation for magnetic components employed in power electronic systems," *IEEE Trans. Power Electron.*, vol. 27, no. 2, pp. 964–973, Feb. 2012, doi: 10.1109/TPEL.2011.2162252.
[9] S. Barg, K. Ammous, H. Mejbri, and A. Ammous, "An improved empirical formulation for magnetic core losses estimation under nonsinusoidal induction," *IEEE Trans. Power Electron.*, vol. 32, no. 3, pp. 2146–2154, Mar. 2017, doi: 10.1109/TPEL.2016.2555359.
[10] Y. Sakaki, M. Yoshida, and T. Sato, "Formula for dynamic power loss in ferrite cores taking into account displacement current," *IEEE Trans. Magn.*, vol. 29, no. 6, pp. 3517–3519, Nov. 1993.
[11] M. Luo, D. Dujic, and J. Allmeling, "Modeling frequency independent hysteresis effects of ferrite core materials using permeance–capacitance analogy for system-level circuit simulations," *IEEE Trans. Power Electron.*, vol. 33, no. 12, pp. 10055–10070, Dec. 2018, doi: 10.1109/TPEL.2018.2809704.
[12] M. Luo, D. Dujic, and J. Allmeling, "Modeling frequency-dependent core loss of ferrite materials using permeance–capacitance analogy for system-level circuit simulations," *IEEE Trans. Power Electron.*, vol. 34, no. 4, pp. 3658–3676, Apr. 2019, doi: 10.1109/TPEL.2018.2854874.
[13] H. Cui and K. D. T. Ngo, "Transient core-loss simulation for ferrites with nonuniform field in SPICE," *IEEE Trans. Power Electron.*, vol. 34, no. 1, pp. 659–667, Jan. 2019, doi: 10.1109/TPEL.2018.2812856.
[14] F. Corti, A. Reatti, E. Cardeli, A. Faba, and H. Rimal, "Improved spice simulation of dynamic core losses for ferrites with non-uniform field and its experimental validation," *IEEE Trans. Ind. Electron.*, vol. 68, no. 12, pp. 12069–12078, Dec. 2021.
[15] H. Saotome and Y. Sakaki, "Iron loss analysis of Mn–Zn ferrite cores," *IEEE Trans. Magn.*, vol. 33, no. 1, pp. 728–734, Jan. 1997, doi: 10.1109/20.560105.
[16] O. Bottauscio, M. Chiampi, and A. Manzin, "Influence of constitutive parameters in soft ferrites: A modeling analysis by homogenization technique," *J. Magnetism Magn. Mater.*, vol. 304, no. 2, pp. e746–e748, 2006.
[17] M. T. Johnson and E. G. Visser, "A coherent model for the complex permeability in polycrystalline ferrites," *IEEE Trans. Magn.*, vol. 26, no. 5, pp. 1987–1989, Sep. 1990.

[18] T. Kawano, A. Fujita, and S. Gotoh, "Analysis of power loss at high frequency for MnZn ferrites," *J. Appl. Phys.*, vol. 87, no. 9, pp. 6214–6216, 2000.
[19] T. Nakamura and Y. Okano, "Electromagnetic properties of Mn–Zn ferrite sintered ceramics," *J. Appl. Phys.*, vol. 79, no. 9, pp. 7129–7133, 1996.
[20] W. H. Jeong, Y. H. Han, and B. M. Song, "Effects of grain size on the residual loss of Mn–Zn ferrites," *J. Appl. Phys.*, vol. 91, no. 10, pp. 7619–7621, 2002.
[21] M. Drofenik, A. Žnidaršič, and I. Zajc, "Highly resistive grain boundaries in doped MnZn ferrites for high frequency power supplies," *J. Appl. Phys.*, vol. 82, no. 1, pp. 333–340, 1997.
[22] E. Cardelli, L. Fiorucci, and E. Della Torre, "Estimation of MnZn ferrite core losses in magnetic components at high frequency," *IEEE Trans. Magn.*, vol. 37, no. 4, pp. 2366–2368, Jul. 2001, doi: 10.1109/20.951174.
[23] K. Yee, "Numerical solution of initial boundary value problems involving Maxwell's equations in isotropic media," *IEEE Trans. Antennas Propag.*, vol. 14, no. 3, pp. 302–307, May 1966, doi: 10.1109/TAP.1966.1138693.
[24] P. V. Andrews, M. B. West, and C. R. Robeson, "The effect of grain boundaries on the electrical resistivity of polycrystalline copper and aluminium," *Philos. Mag.*, vol. 19, no. 161, pp. 887–898, 1969.
[25] W. Wu, S. H. Brongersma, M. Van Hove, and K. Maex, "Influence of surface and grain-boundary scattering on the resistivity of copper in reduced dimensions," *Appl. Phys. Lett.*, vol. 84, no. 15, pp. 2838–2840, 2004.
[26] R. C. Munoz and C. Arenas, "Size effects and charge transport in metals: Quantum theory of the resistivity of nanometric metallic structures arising from electron scattering by grain boundaries and by rough surfaces," *Appl. Phys. Rev.*, vol. 4, 2017, Art. no. 011102.
[27] N. J. Peter et al., "Segregation-induced nano faceting transition at an asymmetric tilt grain boundary in copper," *Phys. Rev. Lett.*, vol. 121, no. 25, 2018, Art. no. 255502.
[28] T. Frolov et al., "Grain boundary phases in BCC metals," *Nanoscale*, vol. 10, no. 17, pp. 8253–8268, 2018.
[29] T.-H. Kim et al., "Structural dependence of grain boundary resistivity in copper nanowires," *Jpn. J. Appl. Phys.*, vol. 50, no. 8, 2011, Art. no. 08LB09.
[30] D. G. Brandon, "The structure of high-angle grain boundaries," *Acta Metallurgica*, vol. 14, no. 11, pp. 1479–1484, 1966.
[31] D. Valencia et al., "Grain-boundary resistance in copper interconnects: From an atomistic model to a neural network," *Phys. Rev. Appl.*, vol. 9, 2018, Art. no. 044005.
[32] G. Kim, X. Chai, L. Yu, X. Cheng, and D. S. Gianola, "Daniel, interplay between grain boundary segregation and electrical resistivity in dilute nanocrystalline Cu alloys," *Scr. Mater.*, vol. 123, pp. 113–117, 2016.
[33] J. Budai, W. Gauddig, and L. Sass, "The measurement of grain boundary thickness using X-ray diffraction techniques," *Philos. Mag. A*, vol. 40, pp. 757–767, 2006.
[34] H. P. Rimal et al., "Protection from indirect lightning effects for power converters in avionic environment: Modelling and experimental validation," *IEEE Trans. Ind. Electron.*, vol. 68, no. 9, pp. 7850–7862, Sep. 2021.
[35] H. P. Rimal, A. M. Ghanim, S. Q. Antonio, G. M. Lozito, A. Faba, and E. Cardelli, "Modelling of dynamic losses in soft ferrite cores," *Phys. B, Condens. Matter.*, vol. 579, 2020, Art. no. 411811.
[36] H. P. Rimal, S. Q. Antonio, A. Faba, and E. Cardelli, "Modeling of combined metal oxide varistors and ferrite core filters to augment avionic safety during lightning transients," *IEEE Trans. Electromagn. Compat.*, vol. 62, no. 5, pp. 2012–2023, Oct. 2020.
[37] J. Crank and P. Nicolson, "A practical method for numerical evaluation of solutions of partial differential equations of the heat-conduction type," in *Mathematical Proceedings of the Cambridge Philosophical Society*, vol. 43. Cambridge, U.K.: Cambridge Univ. Press, Jan. 1947, no. 1, pp. 50–67.
[38] A. Faba and H. P. Rimal, "Robust lightning indirect effect protection in avionic diagnostics: Combining inductive blocking devices with metal oxide varistors," *IEEE Trans. Ind. Electron.*, vol. 65, no. 8, pp. 6457–6467, Aug. 2018.
[39] E. C. Snelling, *Soft Ferrites, Properties and Applications*. Iliffe Books Ltd., London, 1969, pp. 162–168.
[40] R. Lewis and V. Torczon, "Pattern search methods for linearly constrained minimization," *SIAM J. Optim.*, vol. 10, no. 3, pp. 917–941, 2000.

Hari Prasad Rimal (Student Member, IEEE) received the bachelor's degree in electrical engineering from Tribhuvan University (TU), Institute of Engineering (IOE), Lalitpur, Nepal, in 2011, the M.Sc. degree in electrical engineering from TU-IOE and Politecnico di Milano, Milan, Italy, in 2015, and the Ph.D. degree in industrial engineering from the University of Perugia, Perugia, Italy, in 2020.

He is currently a Postdoctoral Researcher with the Department of Engineering, University of Perugia. His research interests include power electronics, power systems, and the modeling and characterization of magnetic materials.

Giulia Stornelli received the Mechanical Engineering degree from the University of Roma Tre, Rome, Italy, in 2018. She is currently working toward the Ph.D. degree in industrial engineering from the University of Roma "Tor Vergata," Rome, Italy, with a research activity mainly focused on metallurgy of steel for nuclear fusion applications.

She cooperates with the University of Perugia, Perugia, Italy, on metallurgy issues, mainly for the energy sectors.

Antonio Faba (Senior Member, IEEE) received the Electrical Engineering degree from the University of L'Aquila, L'Aquila, Italy, in 1998, and the Ph.D. degree in industrial engineering from the University of Perugia, Perugia, Italy, in 2006.

He is currently an Associate Professor with the Department of Engineering, University of Perugia, where he is also the Head of the Laboratory of Electromagnetic Characterization.

Dr. Faba is a Member of the IEEE Magnetic Society. He was the receipient of the National Habilitation for Full Professor in 2018.

Ermanno Cardelli (Senior Member, IEEE) received the M.Sc. and Ph.D. degrees in electrical engineering from the University of Pisa, Pisa, Italy, in 1981 and 1987, respectively.

He is currently a Full Professor of electric engineering and the Head of the Department of Engineering with the University of Perugia, Perugia, Italy. He has authored more than 200 refereed technical papers, mainly on numerical techniques and modeling for electromagnetic field analysis. He has also authored two Italian edited books and an international book chapter.

Dr. Cardelli was the Past Chair of the IEEE Italy Section, the Chair of the Electrical Engineering Group, and a Referee and a Guest Editor for international journals. He was the General Chair for several international conferences and a Coordinator of many Italian and European scientific programs.